Nanoscale Advances

ROYAL SOCIETY OF CHEMISTRY

PAPER

View Article Online
View Journal | View Issue

Cite this: *Nanoscale Adv.*, 2021, **3**, 800

An all-inorganic, fully dense, stretchable ceramic magnetic film†

Muchun Liu, *[ab] Lijuan Qian, [c] Chao Yu, [a] Gang Xiao *[c] and Robert H. Hurt *[a]

Received 12th November 2020
Accepted 1st December 2020

DOI: 10.1039/d0na00949k

rsc.li/nanoscale-advances

There is widespread interest in new materials-based approaches for introducing flexibility to electromagnetic devices, such as displays, human–machine interfaces, smart textiles, and biomedical implants. From fabrication to application, incorporating ceramic components is particularly challenging due to their extreme stiffness. Here, we introduce a new approach for designing flexible ceramic films and demonstrate it by fabricating fully dense, pre-wrinkled magnetic cobalt ferrite films composed of tiled nanoplatelets. The method relies on the colloidal engineering of metalized graphene nanosheets, which are cast and compressed into wrinkled composite films with accurate control of composition and morphology. Removal of the graphene template by thermal oxidation yields free-standing cobalt ferrite films that can be stretched up to 200% and bent to radii of 2.5 mm while maintaining their magnetic properties. Magnetization retention of 73% is documented after 150% linear mechanical stretching over 100 cycles. The significant stretchability and flexibility in this hard magnetic material is achieved at near full metal oxide crystal density without addition of significant void space or a polymeric elastomer matrix.

Introduction

Flexible and stretchable devices are becoming essential components in next-generation technologies that include electronic displays, soft robotics, electronic skins, smart textiles, batteries and supercapacitors for energy storage, and functional biomedical implants.[1–4] Imparting flexibility and stretchability often pose significant materials science challenges and most approaches often fall in one of two classes: compositional design and structural design. Compositional design involves replacing rigid material components with flexible alternatives, such as conductive polymers, carbon nanotubes, and graphene-based materials.[5–7] In contrast, the structural design approach retains the traditional focus on hard material components but manipulates their physical form and structure to allow device deformation, for example through thickness reduction (*e.g.* Ag nanowires, nanoribbons, flexible hard metal magnetic films), engineered wavy structures (*e.g.* buckled Si films) or open mesh geometries such as patterned arrays of metallic interconnects.[2,8] Some functional materials, however, cannot be simply replaced or effectively re-shaped, and ceramics components are often particularly challenging due to extreme stiffness and brittleness.

Ceramic materials that serve as semiconductors (In_2O_3/ZnO, SiC), insulators (Si_3N_4), catalysts (Al_2O_3, Fe_2O_3) or magnetic nanoparticles ($CoFe_2O_4$) can be essential in emerging devices[3,9] Ceramics, however, typically fracture at low strain (typically 0.1–0.2%), which can pose a significant challenge for engineering flexibility and stretchability.[10,11] For this reason, most ceramic components are incorporated in devices as nano/micro-scale dispersed phases encapsulated in soft matrices and or integrated through stretchable interconnects that accommodate the primary stress during deformation.[12–15] The use of the flexible matrix results in lower loading of active material and diminished device performance and/or challenges in processing and the potential for interfacial failure.[16,17]

Here we propose and evaluate a concept for structural design of flexible and stretchable magnetic ceramic metal oxide films that do not involve an elastomeric matrix yet express full density of the inorganic active component. The concept is based on our previous work creating 1D, 2D and hierarchical wrinkle topographies in graphene-based films,[18] and using them as sacrificial templates to self-assemble wrinkled films of other inorganic compositions.[19] In this method, hybrid metal–graphene oxide (GO) nanosheets are colloidally engineered into stable inks that can be written onto substrates to form GO nanosheet films with high densities of metal ions confined in the 2D gallery spaces. In-plane compression of these metallized graphene films produces wrinkles, crumples or complex architectures[18] that can be calcined to oxidize graphene and assemble tiled metal

[a]*School of Engineering, Brown University, Providence, RI, 02912, USA. E-mail: robert_hurt@brown.edu*

[b]*Department of Civil and Environmental Engineering, Massachusetts Institute of Technology, Cambridge, MA, 02139, USA. E-mail: muchunl@mit.edu*

[c]*Department of Physics, Brown University, Providence, RI, 02912, USA. E-mail: gang_xiao@brown.edu*

† Electronic supplementary information (ESI) available. See DOI: 10.1039/d0na00949k

oxide films that retain the wrinkled microtexture. In the present study, we synthesized pre-wrinkled films of cobalt ferrite ($CoFe_2O_4$) – a ferrimagnetic ceramic – and characterized their flexibility, stretchability, and magnetic properties, as well as the stability of those magnetic properties during multiple flex/stretch cycles.

Experimental

Materials

Ethanol, iron(III) nitrate nonahydrate ($Fe(NO_3)_3 \cdot 9H_2O$), cobalt(II) nitrate hexahydrate ($Co(NO_3)_2 \cdot 6H_2O$), anhydrous acetone and methylene chloride were purchased from Sigma-Aldrich. GO was synthesized by a modified Hummers' method as reported before.[20] Thermally responsive polystyrene heat shrink films were purchased from Grafix. Polydimethylsiloxane (PDMS) was made from a SYLGARD 184 silicone elastomer kit. All water was deionized (18.2 MΩ, milli-Q pore). All reagents were used as received without further purification.

Procedures

Fabrication of wrinkled GO films. The as-synthesized GO nanosheets had nominal lateral sizes ~1 μm and thickness values ~1 nm based on SEM and AFM data shown in Fig. S1.† The GO suspensions used for colloidal phase measurement and film casting had a solid loading of 1 mg mL^{-1}, with a C/O atomic ratio of ~2.1.[20,21] Potential GO impurities such as N, S, Mn, K, Cl, and P were not detected by XPS. The polystyrene shrink film was cut into 1.5 × 4.0 cm^2 rectangles and washed with ethanol. Once dry, they were treated in an air plasma using a Deiner Atto standard plasma system with a borosilicate glass chamber and a 13.56 MHz, 0–50 W generator. The chamber pressure was pumped down to and maintained at 0.13 mbar while flushing with air for 5 min. Plasma was then generated at 100% power (50 W) for 15 min followed by slow venting of the chamber. 300 μL of GO 1 mg mL^{-1} suspension was drop cast onto each 1.5 × 4.0 cm^2 polystyrene substrate. After 60 °C oven drying, two opposing sides of each polystyrene substrate were clamped to prevent contraction along one axis. The GO coated polystyrene substrates were then put in 130 °C oven for 6 min to achieve uniaxial contraction along the other axis.

Fabrication of SMOFs (stretchable metal oxide films). GO aqueous suspensions (1 mg mL^{-1}) were well mixed with 4 mM $Fe(NO_3)_3$ and 2 mM $Co(NO_3)_2$ aqueous solutions. 300 μL of the mixture was drop cast onto 1.5 × 4.0 cm^2 plasma treated polystyrene substrate. After 60 °C oven drying, the samples were dried and heated to activate shrinkage as described above. The samples were then immersed in methylene chloride to fully dissolve the polystyrene substrate and washed with acetone. The resulting free-standing GO–Fe(III)/Co(II) wrinkled films were carefully collected from the acetone. Dried GO–Fe(III)/Co(II) wrinkled films were calcined at 600 °C in air for 2 h to obtain SMOFs.

Preparation of SMOFs attached to PDMS substrates. PDMS was made from a SYLGARD 184 silicone elastomer kit. It is composed of a base/curing agent to be manually mixed in a 10 : 1 weight ratio (base to curing agent). Here 1.75 g of the base/curing agent mixture was poured into an aluminum dish under vacuum for 15 minutes, then placed in a 60 °C oven for 14 minutes. When the PDMS was partially cured to a gel phase, a SMOF was gently placed on the surface of PDMS. The highly viscous PDMS gel conformally deformed along and supported the wrinkles of SMOF. The mixture was put back into 60 °C oven for another 20 minutes to stabilize the adhesion of PDMS and prevent the immersion of SMOF.

Stretching/bending deformation of SMOFs. Stretching behavior was characterized by pulling the PDMS-supported SMOFs along the wrinkling direction (perpendicular to the ridge lines) to pre-selected strain values and then clamping on a metal plate with calibration lines. The plate was placed in a 130 °C oven to further harden the PDMS and "freeze" the strain prior to characterization of the deformed film (see below). Bending behavior was characterized by wrapping the PDMS/SMOFs composite around aluminum columns of selected diameter, then placing in a 130 °C oven to harden the PDMS and "freeze" in the deformation prior to structural characterization (below).

Material and film characterization. The surface morphologies of GO and SMOFs were investigated using a field emission SEM (LEO 1530 VP) operating at 10.0 kV for imaging. Before SEM imaging, all samples were coated with a layer of AuPd (<1 nm). Surface morphology and thickness of GO nanosheets were also characterized by AFM (Asylum MFP-3D Origin) operating in alternating contact mode. TEM and SAED were performed using a JEOL 2100F TEM/STEM at an acceleration voltage of 200 kV, equipped with an energy dispersive X-ray spectrometer for elemental analysis. All samples were suspended in ethanol for 30 min of sonication, then dropped on lacey carbon grids for observation. TGA were carried out on a METTLER TOLEDO TGA/DSC 1 STARe system, with heating rate of 10 °C min^{-1}, air flow of 80 mL min^{-1}, and sample mass of ~1 mg. The compositions and phases of as-prepared metal oxide products were identified by XRD on a Bruker D8 Discovery 2D X-ray Diffractometer with Cu Kα radiation (λ = 1.5418 Å). Magnetic measurements were carried out using a Quantum Design® Physical Property Measurement System (PPMS).

Results and discussion

Fig. 1a illustrates the fabrication route for SMOF adapted from our previously reported method.[19] Briefly, a GO–Fe(III)/Co(II) solution/suspension is drop cast onto thermally responsive polystyrene substrates. Heating actuates substrate contraction, and the resulting compression and periodic folding of the top film is restricted to one dimension by physical fixation of the substrate on two opposing ends. The wrinkled GO–Fe(III)/Co(II) coating is then calcined under 600 °C to remove the graphene template and release a free standing SMOF. Note that the GO nanosheets are used as sacrificial templates to create arrays of ultrathin 2D reaction chambers, but are not retained in the final product. The encapsulated metal ions originally confined in the 2D gallery spaces are converted to continuous tiled polycrystalline ceramic films by a self-assembly process that

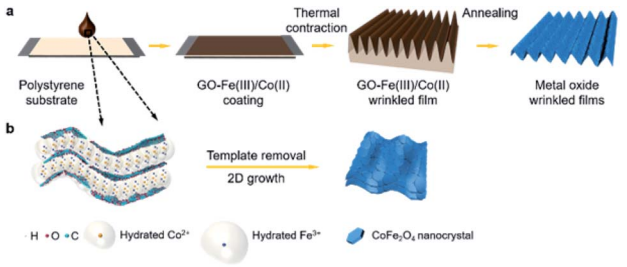

Fig. 1 Detailed fabrication process for stretchable metal oxide wrinkled films (SMOFs). (a) SMOFs fabricated by conformal coating and uniaxial contraction of GO–Fe(III)/Co(II) suspension on polystyrene substrate. Heating above glass transition temperature ($T_g \sim 100$ °C) triggers polymer relaxation to produce wrinkled textures. The film is calcined at 600 °C to oxidatively remove graphene and convert metal ions to a tiled metal oxide polycrystalline film. (b) Sketch of conversion of GO–Fe(III)/Co(II) suspension to $CoFe_2O_4$ film with tessellation structure.

replicates the original graphene textures at high fidelity (Fig. 1b). X-ray diffraction (XRD) shows a single phase of Co_2FeO_4 (Fig. S2†). Thermogravimetric analysis (TGA) reveals the sequence of chemical events as the composite is heated, which begin with metal salt decomposition, then GO to reduced GO thermal conversion (partially overlapping with salt decomposition), and then a late removal of the graphene-like reduced GO through O_2 reaction above 450 °C (Fig. S3†).

Detailed morphologies of the SMOFs are shown in Fig. 2. In the free standing state, SMOFs exhibit the dark brown color of Co_2FeO_4 (Fig. 2a). On the microscale, SMOFs replicate the characteristic GO wrinkle texture – continuous out-of-plane undulations – in a unidirectional pattern with wavelength of ~5 μm (Fig. 2 and S4†). Fig. 2b and c show an example cross-section of SMOFs, which contains ~3 layers with each layer having a thickness ~30 nm. The multi-layer structure of the SMOF likely arises from the layered structure of the GO template though the SMOF shows much smaller layer number indicating *Z*-directional consolidation during the complex decomposition and assembly process. The surfaces of the SMOF show tessellated nanoplatelets ~150 nm in lateral size, arranged as in a mathematical tessellation (Fig. 2d). The constituent nanoplatelets are not isotropic nanoparticles, but have plate-like geometries and smooth top surfaces that reflect 2D crystal growth. From Fig. S5† we can see the primary crystal growth direction of the Co_2FeO_4 nanoplatelets is [011].

Fig. 3a shows the stretching behavior of the stretchable metal oxide films. We used a similar technique to our previous work on pure GO,[22] in which crumpled GO films were attached to an elastomeric substrate and expanded to 1500% areal strain for 500 cycles. Here SMOFs were attached to the top of PDMS substrates and slowly stretched to strains of 50, 100, 150 and 200%. We observed no obvious cracks at or below 100% strain, which is remarkable since cobalt ferrite has no significant intrinsic elasticity on this scale. Micro cracks initiated on the ridges at 150% strain, then propagated at 200% (Fig. 3b). The wavelengths of wrinkles in samples increased from 5 (at 0% strain) to 10 (at 50%), 15 (at 100%), 25 (at 150%) and 35 μm (at 200% strain). In the simple case where all N wrinkles are preserved, the wavelength is $\sim L/N$ (L as the total length) and should grow proportionally to L during stretching. The faster increase in wavelength observed in the present data may be explained by the heterogeneous nature of the wrinkles and the disappearance of secondary wrinkles at high strain leading to local doubling. The height of SMOF decreased from ~6 μm to 150 nm (the thickness of planar metal oxide film) at 150% strain. We used a vibrating-sample magnetometer (VSM) to probe the magnetic properties of the films and their stress coupling (Fig. 3c). The saturation magnetization (M_s) and remnant magnetization (M_r) of SMOF along the *x*-axis (parallel to the wrinkles) are ~50 and 15 emu per g, and remain stable

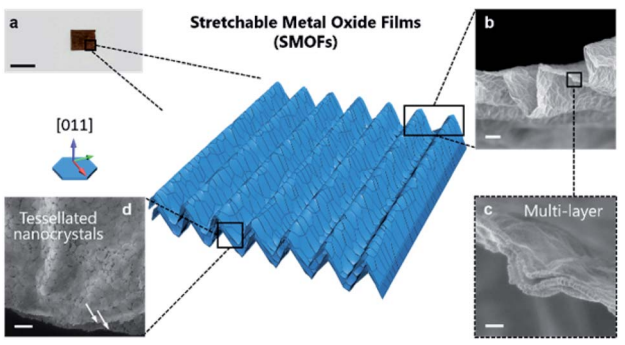

Fig. 2 Morphologies of SMOFs. (a) Optical photo of a free-standing SMOF. Scale bar, 0.4 cm. (b) Cross-section of SMOF. From the side view, SMOF exhibits undulate structures, with a film thickness of ~150 nm. Scale bar, 5 μm. (c) Enlarged side view of SMOF, exhibiting layered structure with single layer thickness ~30 nm. Scale bar, 200 nm. (d) Top view of SMOF, with multiple layers exposed on edge (white arrows). Each layer is constructed of tessellated nanoplatelets with lateral size ~150 nm. Scale bar, 200 nm. The primary crystal orientation of the nanoplatelets is [011].

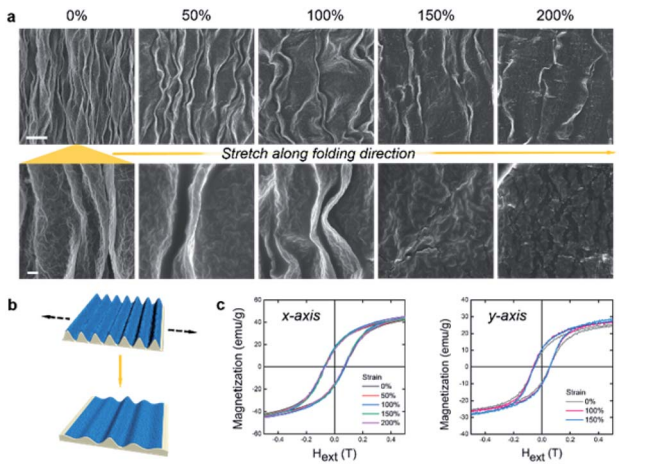

Fig. 3 Stretchability: morphology and magnetic properties of SMOFs under tensile strain. (a) Surface morphologies of SMOFs at observed strains of 0–200%, magnified images are shown in bottom row. Scale bar, 20 μm (top row), 2 μm (bottom row). (b) Illustration of the bending process of SMOF. (c) Magnetic properties of SMOFs as a function of unidirectional strain along *x*- and *y*-axis.

under strains up to 200% at room temperature. The M_s along the *y*-axis (perpendicular to the wrinkles) shows a 10% increase at 150% strain, which may be caused by the restoration of the shape anisotropy in the SMOF. The M_r along *x*- or *y*-axis shows insignificant change during stretching (Fig. S6a and b†). No scaling of nanocrystals was observed upon stretching, and therefore, SMOF shows high stretchability and stable magnetic properties.

The flexibility of SMOFs was studied by again adhering the films on PDMS substrates and now wrapping the composite around aluminum columns with radii of 10.0, 5.0 and 2.5 mm. Fig. 4a shows that bending had little effect on SMOF surface morphologies, and SEM images revealed no cracks appearing as a result of the bend deformation. Over one wrinkle wavelength, the angle caused by bending is quite small (3×10^{-2}, 6×10^{-2} or 0.1 degrees, at bending radii of 10.0, 5.0 or 2.5 mm) comparing with the local deformation angles built into the wrinkles (~6 × 10 degrees). The high density of wrinkles on curved surfaces mitigates the stress concentration. Therefore, the microstructure of SMOF facilitates its adaptation to different types of macroscale mechanical deformation. The magnetic behaviors of SMOFs remain quite stable under bending strain (Fig. 4b and c). The M_s of SMOF is ~30 emu per g irrespective of bending strain. The M_r along *x*-axis also remains stable during bending (Fig. S6c†).

Fig. 5a and b shows the temperature dependence of SMOF magnetic properties. Increasing temperature from 200 to 380 K, causes a slight decrease in M_s from 52 to 44 emu per g, which is consistent with a previous report that the Curie temperature, T_c ~ 800 K in Co_2FeO_4.[23] The coercive field, H_c, is strongly dependent on temperature, decreasing 10 fold from 0.268 to 0.0265 T as temperature rises from 200 to 380 K. Both coercivity and remnant magnetization decrease with increasing temperature, indicating a decrease in anisotropy along the *x*-axis (parallel to wrinkles) due to the thermal energy. The directional dependence of the hysteresis was measured along the *x*-axis (parallel to wrinkles), *y*-axis (perpendicular to wrinkles) and *z*-axis (perpendicular to the film plane). The *M vs. H* relationships are similar along the three axes (Fig. 5c) but M_r is 20% larger along the *x*-axis than the *y*- and *z*-axes. In general, a random distribution of the magnetocrystalline anisotropy in each nanoplatelet leads to similar behavior along the *x*- and *y*-axes (both are stronger than *z*-axes).[24] The wavy topography of the wrinkled films provides an undulate surface along the *y*-axes, which disturbs the shape anisotropy in the SMOF and results in slightly decreased M_r. Finally, a mechanical fatigue test was conducted by stretching a SMOF to 150% strain over 100 times. Comparison of magnetization is shown in Fig. 5d and e, the M_s decreased to 73% of original after fatigue.

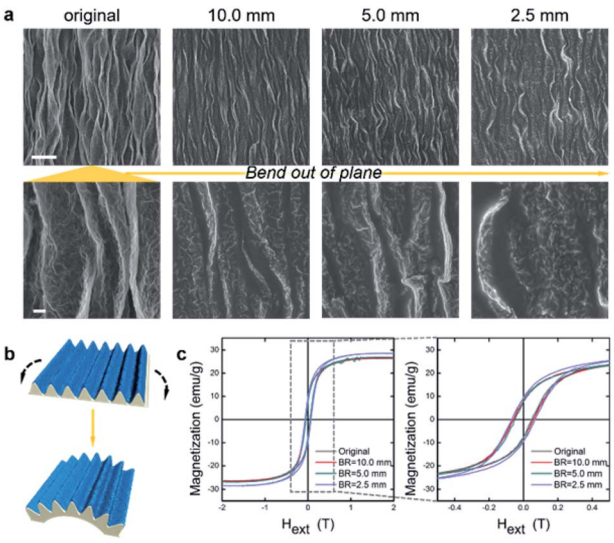

Fig. 4 Flexibility: morphology and magnetic properties of SMOF under bending strain. (a) Surface morphologies of SMOF under bend radii (infinity (planar), 10, 5 and 2.5 mm), magnified images are shown in bottom row. Scale bar, 20 μm (top row), 2 μm (bottom row). (b) Illustration of the bending process of SMOF. (c) Magnetic properties of SMOF at different bend radii along *x*-axis.

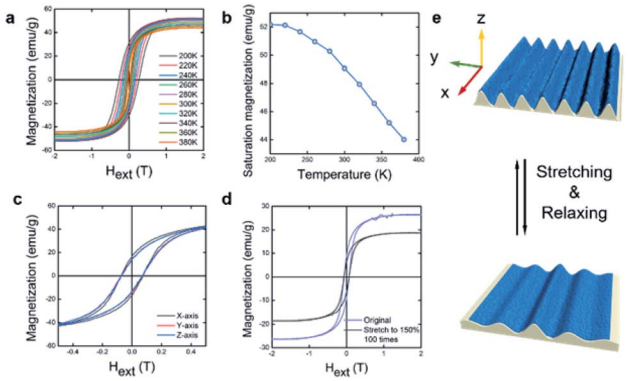

Fig. 5 Temperature dependence, shape anisotropy and mechanical fatigue effects on magnetic behavior of SMOF. (a) The hysteresis loop of SMOF at different temperatures ranging from 200 to 380 K. (b) Temperature dependence of saturation magnetization of SMOF. (c) Magnetization of SMOF along the *x* (parallel to wrinkles), *y* (perpendicular to wrinkles) and *z* directions. (d) Magnetization of SMOF before and after 100 cycles of stretching and relaxing between 0% and 150% strain. (e) Schematic of reversible stretching of a SMOF.

Overall, the key concept in this study is to fabricate a fully dense, geometrically stretchable metal oxide film, in a simple templating method, to produce wrinkled ceramic magnetic film. The technique accomplishes a densely packed nanocrystal tessellation with outstanding mechanical behaviors. The stable magnetic performance of SMOFs during stretching or bending is promising in stretchability-oriented applications.[2,25,26] However, potential correlation between mechanical strain and magnetic properties may be expected through future investigation including tuning of wrinkling wavelength, surface roughness or size/orientation of nanocrystals.[24,27]

Conclusions

Here we synthesized and characterized a stretchable, flexible, magnetic $CoFe_2O_4$ film without the use of polymer matrices by a 2D self-assembly method using textured graphene templating. The final films achieve high stretchability (200% strain) and

flexibility (2.5 mm bending radius) while maintaining stable magnetic performance. The synthesis approach uses simple, scalable aqueous film casting technique and may be extendable to other hard magnetic materials. This work demonstrates a new and alternative approach for incorporating brittle ceramic components in flexible or stretchable devices being currently developed for wearable, implantable, skin-mounted, or hand-held technologies.

Conflicts of interest

The authors have no conflicts to declare.

Acknowledgements

The authors thank Prof. P. Y. Chen from University of Maryland, College Park for helpful discussions and acknowledge financial support from an OVPR Research Seed Award from Brown University.

References

1 S. Xu, Y. Zhang, J. Cho, J. Lee, X. Huang, L. Jia, J. A. Fan, Y. Su, J. Su, H. Zhang, H. Cheng, B. Lu, C. Yu, C. Chuang, T.-i. Kim, T. Song, K. Shigeta, S. Kang, C. Dagdeviren, I. Petrov, P. V. Braun, Y. Huang, U. Paik and J. A. Rogers, *Nat. Commun.*, 2013, **4**, 1543.
2 J. H. Koo, D. C. Kim, H. J. Shim, T.-H. Kim and D.-H. Kim, *Adv. Funct. Mater.*, 2018, **28**, 1801834.
3 W. A. D. M. Jayathilaka, K. Qi, Y. Qin, A. Chinnappan, W. Serrano-García, C. Baskar, H. Wang, J. He, S. Cui, S. W. Thomas and S. Ramakrishna, *Adv. Mater.*, 2019, **31**, 1805921.
4 M. Melzer, D. Makarov and O. G. Schmidt, *J. Phys. D: Appl. Phys.*, 2019, **53**, 083002.
5 J. Mun, J. Kang, Y. Zheng, S. Luo, H.-C. Wu, N. Matsuhisa, J. Xu, G.-J. N. Wang, Y. Yun, G. Xue, J. B. H. Tok and Z. Bao, *Adv. Mater.*, 2019, **31**, 1903912.
6 T. Kim, M. Cho and K. J. Yu, *Materials*, 2018, **11**, 1163.
7 H. Jang, Y. J. Park, X. Chen, T. Das, M.-S. Kim and J.-H. Ahn, *Adv. Mater.*, 2016, **28**, 4184–4202.
8 D.-H. Kim and J. A. Rogers, *Adv. Mater.*, 2008, **20**, 4887–4892.
9 J. A. Rogers, T. Someya and Y. Huang, *Science*, 2010, **327**, 1603.
10 D. J. Green, *An Introduction to the Mechanical Properties of Ceramics*, Cambridge University Press, Cambridge, 1998.
11 S. G. Seshadri and K. Y. Chila, *J. Am. Ceram. Soc.*, 1987, **70**, C-242–C-244.
12 K. Sim, Z. Rao, Z. Zou, F. Ershad, J. Lei, A. Thukral, J. Chen, Q.-A. Huang, J. Xiao and C. Yu, *Sci. Adv.*, 2019, **5**, eaav9653.
13 T. Koshi and E. Iwase, Stretchable Electronic Device with Repeat Self-Healing Ability of Metal Wire, *2017 IEEE 30th International Conference on Micro Electro Mechanical Systems (MEMS)*, 2017, pp. 262–265.
14 J. van den Brand, M. de Kok, A. Sridhar, M. Cauwe, R. Verplancke, F. Bossuyt, J. de Baets and J. Vanfleteren, Flexible and Stretchable Electronics for Wearable Healthcare, *2014 44th, European Solid State Device Research Conference (ESSDERC)*, 2014, pp. 206–209.
15 N. Lazarus, C. D. Meyer, S. S. Bedair, G. A. Slipher and I. M. Kierzewski, *ACS Appl. Mater. Interfaces*, 2015, **7**, 10080–10084.
16 Y. Iwata and E. Iwase, Stress-Free Stretchable Electronic Device Using Folding Deformation, *2017 IEEE 30th International Conference on Micro Electro Mechanical Systems (MEMS)*, 2017, pp. 231–234.
17 S. Lee, Y. Song, Y. Ko, Y. Ko, J. Ko, C. H. Kwon, J. Huh, S.-W. Kim, B. Yeom and J. Cho, *Adv. Mater.*, 2020, **32**, 1906460.
18 P.-Y. Chen, J. Sodhi, Y. Qiu, T. M. Valentin, R. S. Steinberg, Z. Wang, R. H. Hurt and I. Y. Wong, *Adv. Mater.*, 2016, **28**, 3564–3571.
19 M. Liu, P.-Y. Chen and R. H. Hurt, *Adv. Mater.*, 2018, **30**, 1705080.
20 Y. Qiu, S. Moore, R. Hurt and I. Külaots, *Carbon*, 2017, **111**, 651–657.
21 F. Kim, J. Luo, R. Cruz-Silva, L. J. Cote, K. Sohn and J. Huang, *Adv. Funct. Mater.*, 2010, **20**, 2867–2873.
22 P.-Y. Chen, M. Zhang, M. Liu, I. Y. Wong and R. H. Hurt, *ACS Nano*, 2018, **12**, 234–244.
23 D. S. Mathew and R.-S. Juang, *Chem. Eng.*, 2007, **129**, 51–65.
24 M. T. Johnson, P. J. H. Bloemen, F. J. A. d. Broeder and J. J. d. Vries, *Rep. Prog. Phys.*, 1996, **59**, 1409–1458.
25 B. Wang, A. Thukral, Z. Xie, L. Liu, X. Zhang, W. Huang, X. Yu, C. Yu, T. J. Marks and A. Facchetti, *Nat. Commun.*, 2020, **11**, 2405.
26 F. Li, H. Zhao, Y. Yue, Z. Yang, Y. Zhang and L. Guo, *ACS Nano*, 2019, **13**, 4191–4198.
27 S. Monso, B. Rodmacq, S. Auffret, G. Casali, F. Fettar, B. Gilles, B. Dieny and P. Boyer, *Appl. Phys. Lett.*, 2002, **80**, 4157–4159.